Electronic Supplementary Information for:

Mechanochemically-tuned structural annealing: a new pathway to enhancing Li-ion intercalation activity in nanosized β_{II} Li_2FeSiO_4

Majid Rasool[a], Hsien-Chieh Chiu[a], Xia Lu[a,b], Frédéric Voisard[a], Raynald Gauvin[a], De-Tong Jiang[c,d], Andrea Paolella[e], Karim Zaghib[e], and George P. Demopoulos*[a]

a. Materials Engineering, McGill University, Montreal, QC H3A 0C5, Canada.

b. School of Materials, Sun Yat-Sen University, Guangzhou 510275, China.

c. Department of Physics, University of Guelph, Guelph, ON N1G 2W1, Canada.

d. Canadian Light Source, Saskatoon, SK S7N 2V3, Canada.

e. Centre d'excellence-ETSE, Hydro-Québec, Varennes, QC, Canada.

*Corresponding author: Phone: 514-398-2046; Fax: 514-398-4492; **ORCID** #0000-0001-8112-5339;

Email: george.demopoulos@mcgill.ca

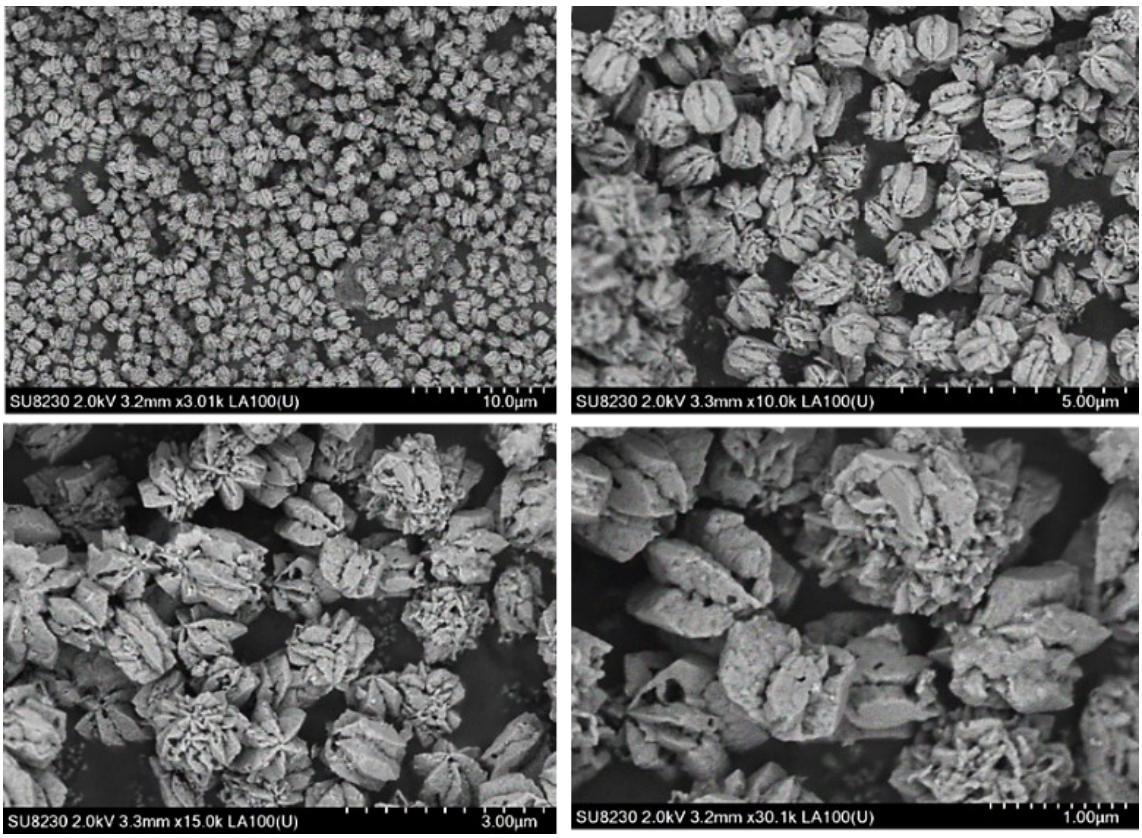

Fig. S1: SEM images of pristine Li_2FeSiO_4 (ortho-LFS) prepared using hydrothermal synthesis at 200°C at different resolutions.

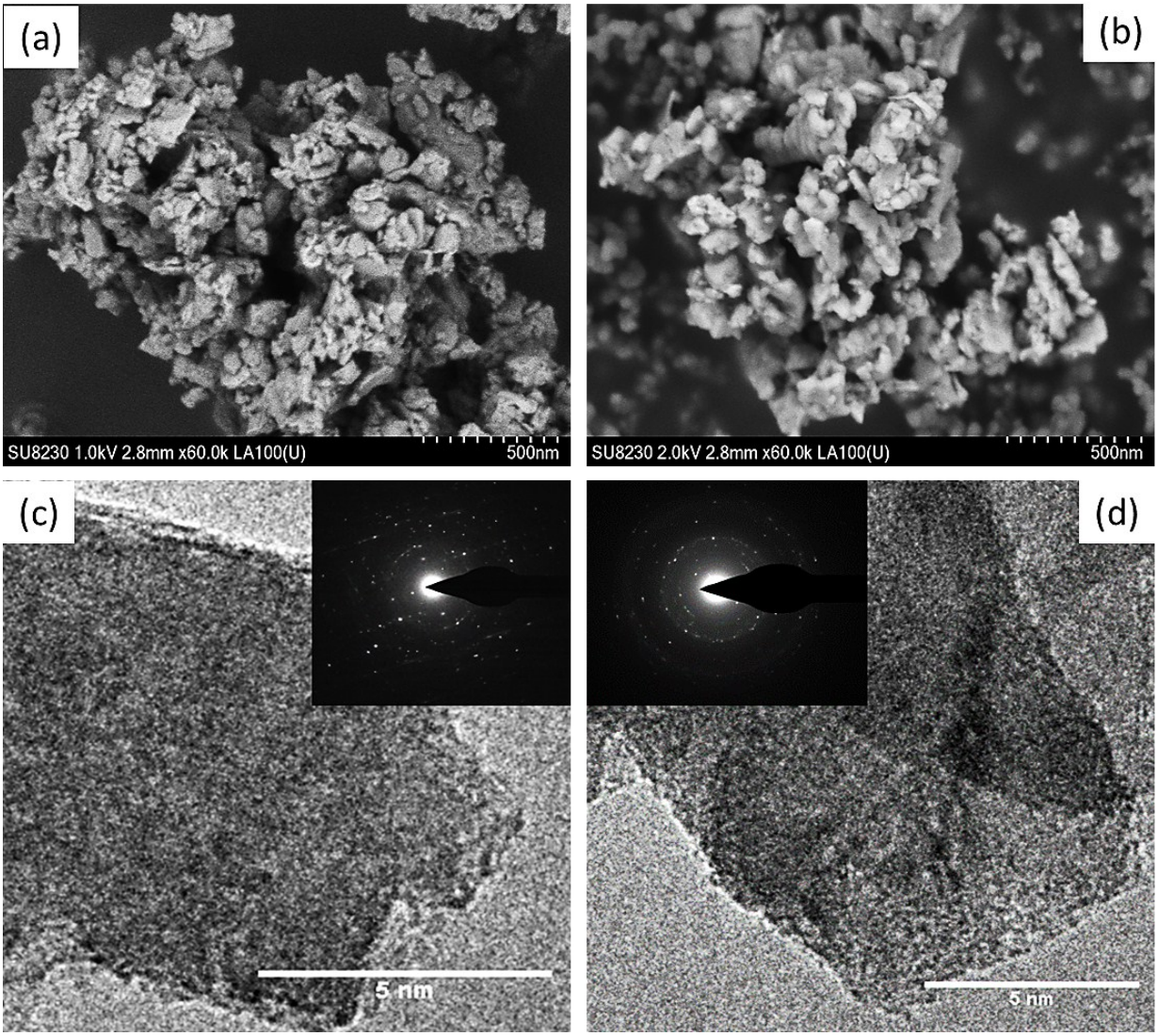

Fig. S2: (a) and (b) SEM images of 8 and 10-h high-energy milled samples, respectively. (c) and (d) HRTEM images of 8 and 10-h high energy milled samples with inset of SAED. Notably, after 10-h of high-energy milling, the material has undergone significant disordering/amorphization as confirmed by XRD analysis (see Fig 2), degree of crystallinity (see Fig. S8) and SAED pattern that shows polycrystalline features (see Fig. S2d), very similar to pristine sample as discussed in the manuscript.

High-energy milling (optimized milling):

To reduce the particle size of Li_2FeSiO_4 (LFS) powder, a Planetary Micro Mill PULVERISETTE 7 premium line (Fritsch) was used**.** Several parameters were checked prior to select the optimized milling conditions mentioned in manuscript. For wet milling, ethanol, methanol and isopropanol were tested as liquid media. However, isopropanol was selected due to its relatively high boiling point (80.37 °C). For milling parameters, several (rotation per minute) RPMs and time durations were tested as shown in the table below:

Table S1: Different milling parameters tested prior to find the "optimized milling" conditions.

RPM	1-hour	3-hour	5-hour	8-hour	10-hour
50	x	x	x	x	X
150	x	x	x	x	x
250	**x**	**x**	**x**	**x**	**x**
350	x	x	x	x	x
450	x	x	x	x	x

For low rpm (50 and 150), the LFS samples had shown agglomerates even after 5-hour milling and no crystal refinement was observed. For 250 rpm, please refer to the manuscript. For high rpm (both 350 and 450 rpm), even after 1-3 hour of milling, the sample began to lose its crystal order and become amorphous, similarly no observation was made for crystal refinement. Therefore, only 250 rpm with different milling time was further analysed and several samples were tested at Canadian Light Source (CLS) for Synchrotron based- XRD analysis as discussed in the manuscript.

BET Analysis:

Fig. S2 shows the Brunauer Emmett-Teller (BET) adsorption curves for different samples. The specific surface area can be determined by physical adsorption of a gas on the surface of the solid (powder sample). The amount of adsorbate gas is calculated which corresponds to a monomolecular layer on the surface. This physical adsorption of gas is due to Van der Waals forces between the adsorbate gas molecules and the adsorbent surface area of the powder sample. The determination is usually carried out at the temperature of liquid nitrogen. As with any theory, there are several assumption made prior to the adsorption calculation i.e. homogeneous surface, local equilibrium, limited molecular interaction etc. [1]. The specific surface area can be calculated from the amount of gas adsorbed by the following equation.

$$S = \frac{V_m NA}{22{,}400 \times m}$$

The constant N is Avogadro's number, V_m is the adsorbed monolayer volume, A is the cross-sectional area of single adsorbed gas molecule, m is the mass of nanomaterials used in the measurement and 22,400 represents the Standard Temperature and Pressure (SSTP) volume of one mole of gas. The extracted specific surface from BET (as shown in Fig. S2) can be used to determine the equivalent spherical particle diameter using the following equation:

$$D_{BET} = \frac{6000}{\rho . S_\omega}$$

Where D_{BET} is the average diameter of a spherical particle, S_ω represents the measured surface area of the powder in $m^2 g^{-1}$, and ρ is the theoretical density in g cm^{-3} [2].

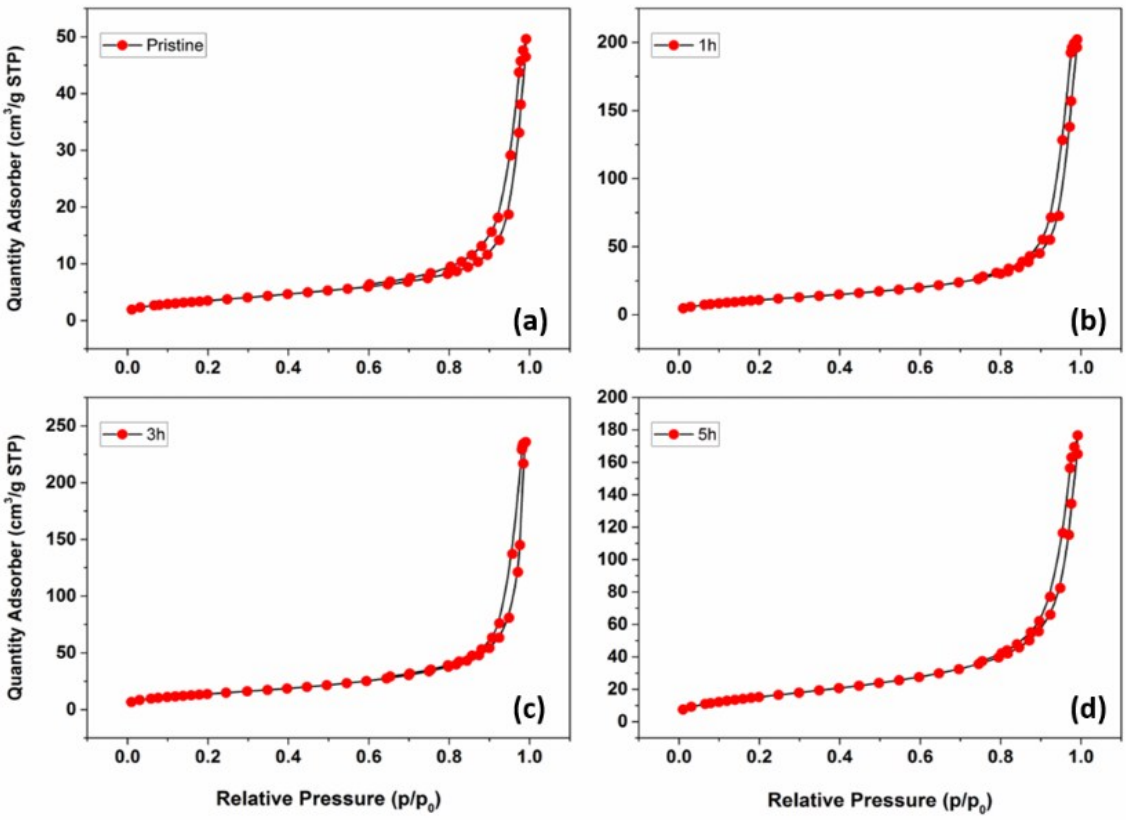

Fig. S3: Nitrogen adsorption-desorption isotherm plots of ortho-LFS samples prepared at different milling times: (a) Pristine, (b) 1-h, (c) 3-h, and (d) 5-h samples.

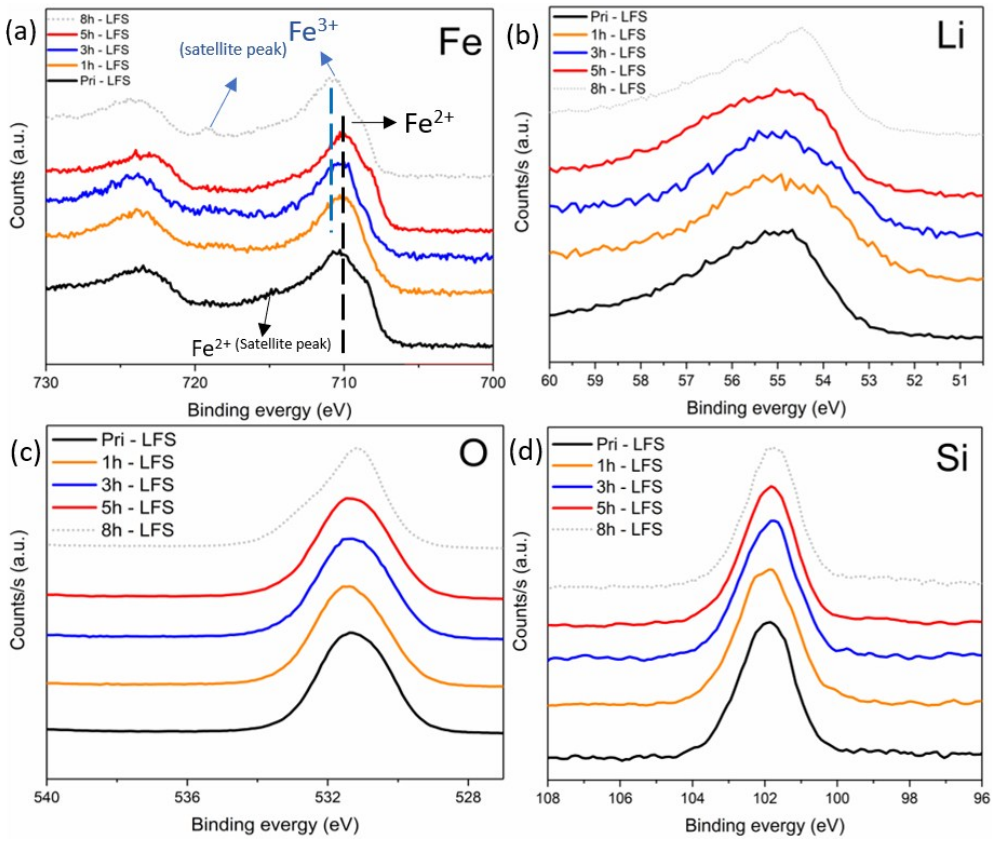

Fig. S4: XPS data collected for various samples before and after high-energy milling. All the spectra were collected for 50 scans and no additional smoothing was performed. Here in (a) the Fe spectra show all the samples to correspond to Fe^{2+} except 8-h sample that corresponds to Fe^{3+}. However minor satellite peaks of Fe^{3+} can be seen for the shorter time (1-h to 5-h) milled samples as more clearly revealed upon data fitting for deconvolution of the spectra in Fig. S5. No trace of Fe^{3+} can be seen for the pristine LFS in Fig. S5. (b) The Li spectra show no new peaks appearing after high-energy milling but only a slight shift after milling (optimized conditions); the 8h-sample is excluded from discussion here due to surface oxidation. (c) O and (d) Si spectra show no new peaks either, i.e. they remain the same even after milling for 8 hours.

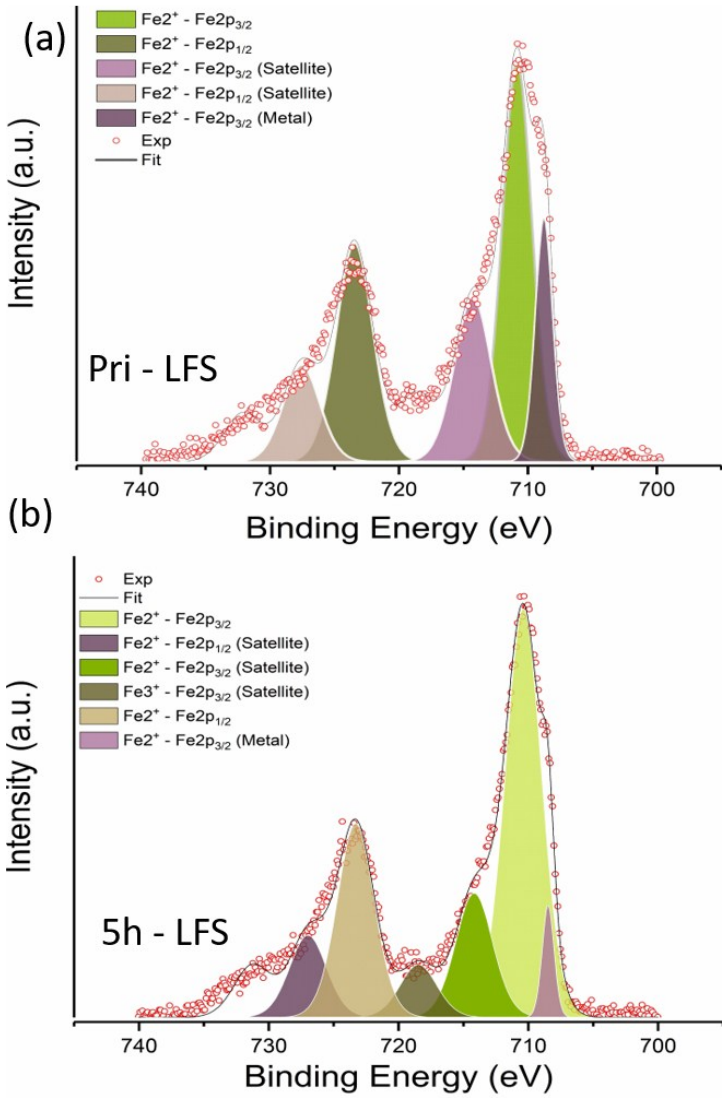

Fig. S5: Deconvolution fitting of XPS iron spectra corresponding to (a) pristine ortho-LFS and (b) 5h-milled LFS; the background was subtracted using *Advantage* software. For pristine sample the iron spectra could be fitted with $Fe2p_{3/2}$, $Fe2p_{1/2}$ and their corresponding satellite peaks. Peaks of $Fe2p_{3/2}$ at 710 eV and $Fe2p_{1/2}$ at 723 eV correspond to Fe^{2+} along with their corresponding satellite peaks. For 5h-LFS sample, Fe^{2+} peak occurred at 710 eV dominates along its satellite peaks but a trace of Fe^{3+} at 718 eV appears to be present.

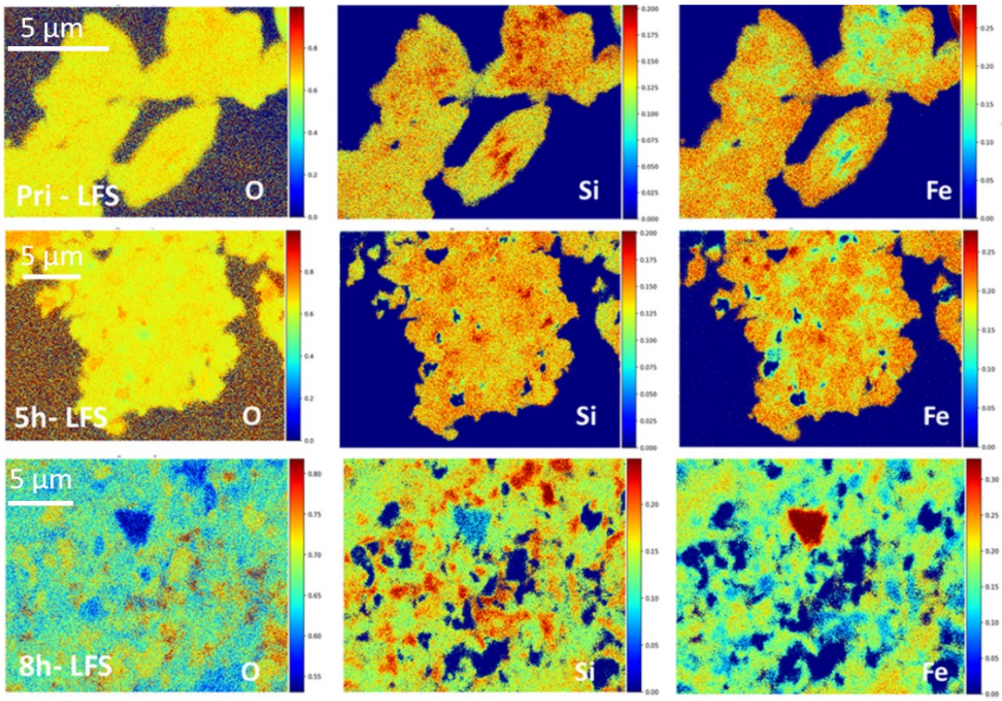

Fig. S6: EDS maps collected to probe the chemical changes induced on the surface before and after high-energy milling. Here f-ratio maps of Oxygen, Silicon and Iron are shown for pristine ortho-LFS, 5-h and 8-h samples, respectively. *f*-Ratio is defined as $f = \frac{I_A}{I_A + I_B}$, where I_A and I_B are the net characteristic X-ray intensities in one spectrum [3]. Oxygen maps for pristine and 5-h sample show homogeneous distribution. By far the biggest surface changes are manifested by the 8-h sample. In this case in addition to the extensive surface oxidation revealed by the presence of Fe^{3+} in the XPS analysis (Figure S4), significant heterogeneous distribution of Fe and Si appears to have occurred possibly due to observed amorphization that is known to be more pronounced near the particle surface [4]. Given that the 8-h milled sample was found to have become predominantly amorphous/disordered characterized by poor intercalation performance no further investigation of it was pursued.

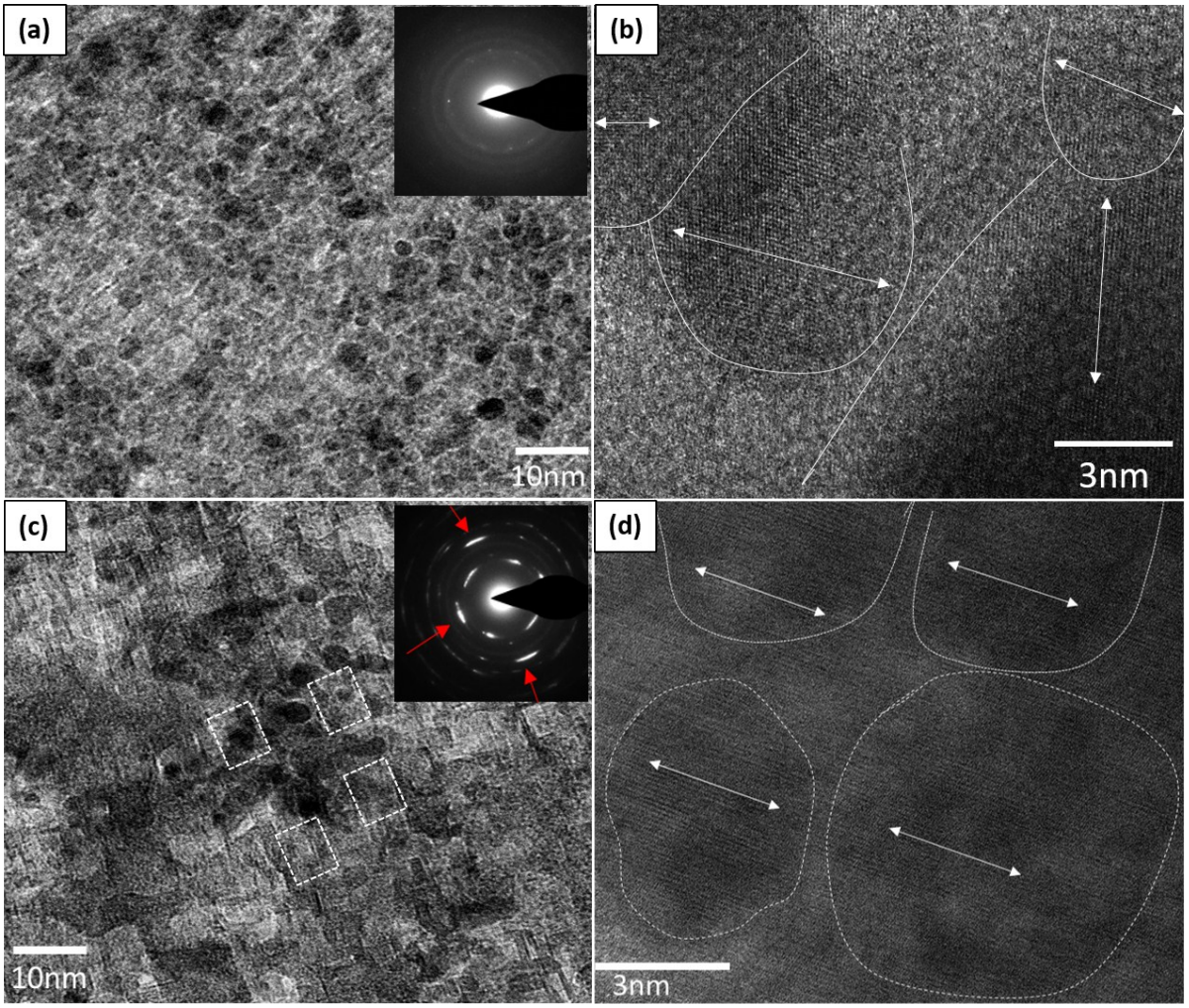

Fig. S7: Fig. S4. A lacy carbon grid was dipped in the slurry of pre-vacuum dried 5-h milled sample for characterization of the primary nanoparticles. (a) TEM image of the initial dried suspension collected after resting for 30 mins showing primary nanoparticles ranging in size from 10 to 15 nm. In inset, SAED shows diffractions rings indicative of polynanocrystals. (b) Corresponding HRTEM image showing lattice planes in these primary nanoparticles with various lattice directions as indicated by arrows and circles along with grain boundaries. (c) TEM image of the 5-h milled material collected after prolonged resting (~24 h). It can be clearly seen the primary nanocrystallites to have developed a self-assembled nanoarchitecture –see rectangles and the corresponding diffraction pattern in SAED image (inset); such diffraction pattern with its spot-like appearance confirms the formation of single nanocrystal architecture [5-6]. (d) Corresponding HRTEM image showing the crystal planes in the same lattice direction/orientation.

Determination of Degree of Crystallinity:

The degree of crystallinity (DOC) was determined by EVA software. Initially the background was manually selected. This background doesn't represent amorphous or crystalline part of the sample. After removing the background, scattering only from crystalline and amorphous part can be determined by creating two patterns for each part. A ghost background was created to evaluate the amorphous region (without diffusing or cutting any crystalline peaks). This ghost amorphous background can be appended, which can be used to compare with the crystalline region of the sample. Therefore, in the final step, the DOC can be calculated using integrated area between the amorphous and crystalline region by the following equation:

$$DOC = \frac{Crystalline\ Area}{Crystalline\ Area + Amorphous\ Area}$$

The weight fraction of amorphous area, W_{amorph} as shown in Fig. S8, can be calculated from:

$$W_{amorph} = 1 - DOC$$

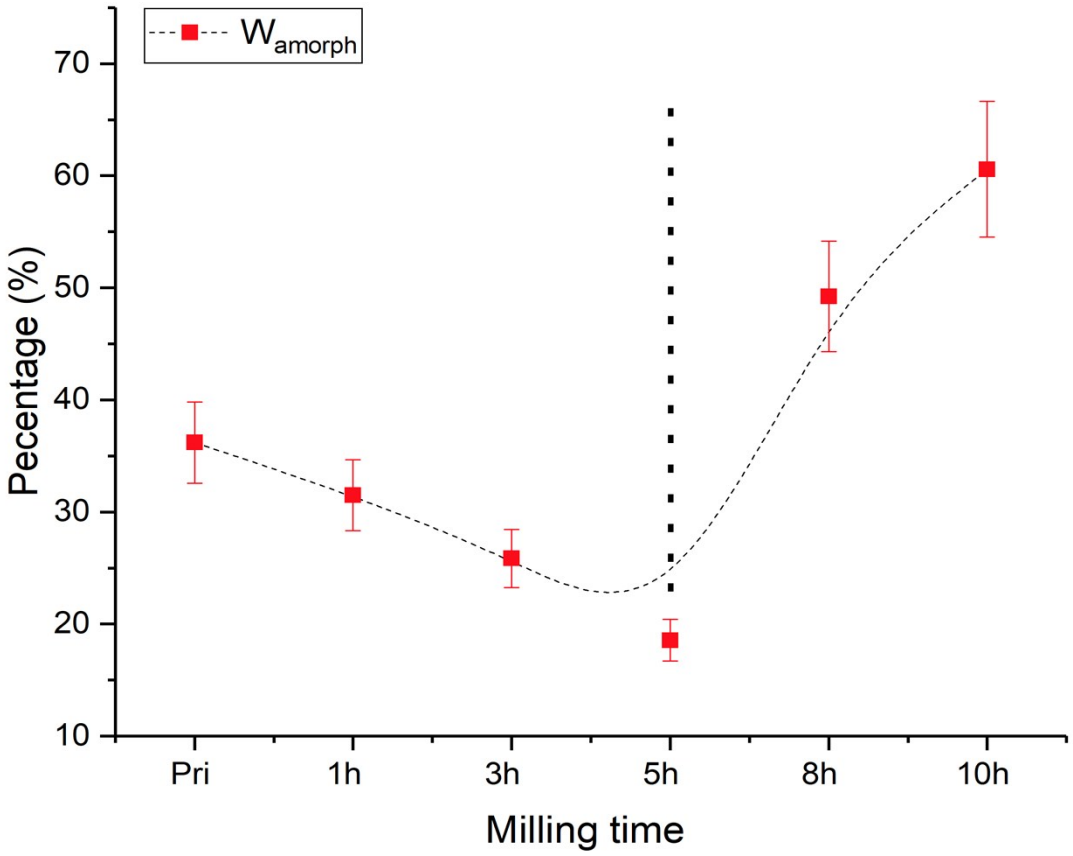

Fig. S8: The weight fraction of amorphous area W_{amorph} for different milled samples at 250 RPM.

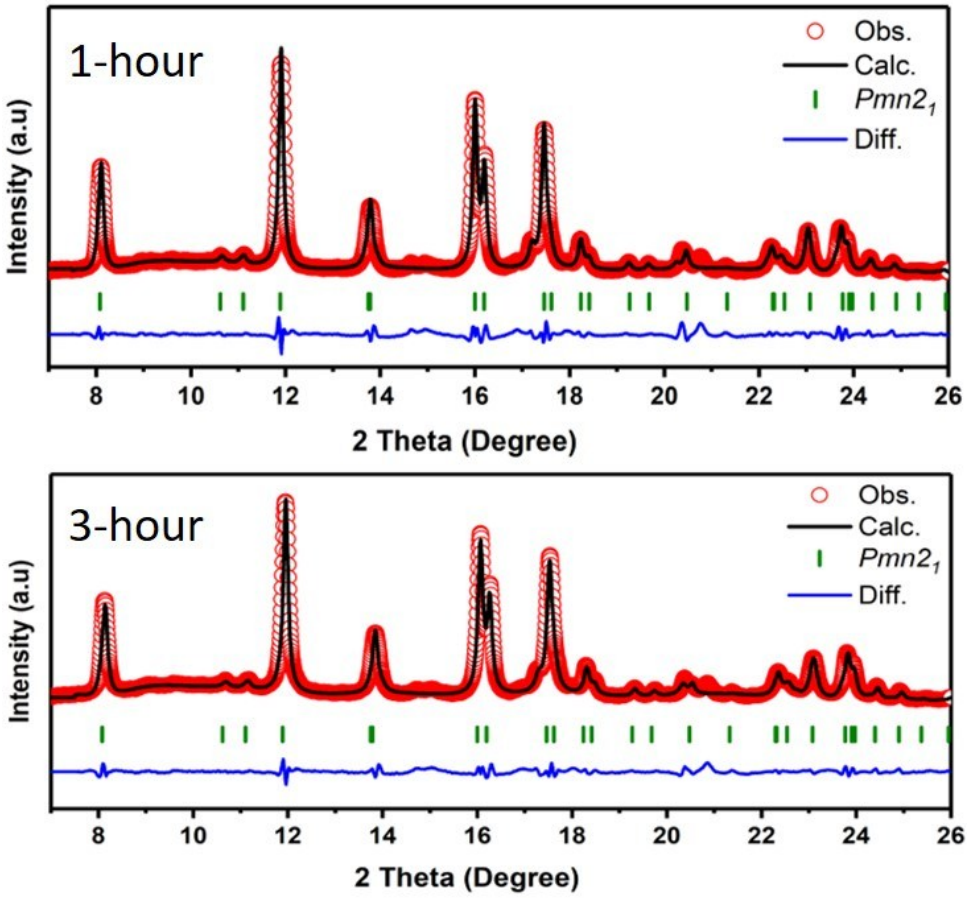

Fig. S9: Top to bottom: 1-h sample was refined with *Pmn2₁* space group with corresponding refinement values of R_{wp}: 3.83, R_p: 2.76 and GOF: 2.37; 3-h milled sample: R_{wp}: 3.81, R_p: 2.90 and GOF: 2.59.

Table S2: Refined crystallographic parameters for (a) pristine Li_2FeSiO_4, (b) 1-h sample, (c) 3-h sample and (d) 5-h sample

(a) Pristine sample

Site	*Np*	*x*	*y*	*z*	*Atom*	*Occ*	*Beq*
Li1	4	0.94078	0.16415	0.77161	Li	0.8125	1
					Fe	0.1875	1
O3	4	0.78850	0.67776	0.89258	O	1	1
Fe1	2	0.00000	0.15270	0.44373	Fe	0.6251	1
					Li	0.3749	1
O1	2	0.00000	0.86603	0.29966	O	1	1
O2	4	0.32465	0.28832	0.79103	O	1	1
Si	2	0.00000	0.82524	0.88782	Si	1	1

Lattice parameters

a (Å)	**6.2691995**
b (Å)	**5.3429072**
c (Å)	**4.9563822**

R_{wp}: 4.60, R_p: 3.51 and GOF: 2.95

(b) 1-h sample

Site	*Np*	*x*	*y*	*z*	*Atom*	*Occ*	*Beq*
Li1	4	1.00000	0.14475	0.76592	Li	0.834	1
					Fe	0.166	1
O3	4	0.76792	0.64786	0.89780	O	1	1
Fe1	2	0.00000	0.16376	0.40531	Fe	0.6679	1
					Li	0.3321	1
O1	2	0.00000	0.83511	0.20163	O	1	1
O2	4	0.29230	0.30180	0.78520	O	1	1
Si	2	0.00000	0.84917	0.83568	Si	1	1

Lattice parameters

a (Å)	**6.2702395**
b (Å)	**5.3425342**
c (Å)	**4.9592315**

R_{wp}: 3.83, R_p: 2.76 and GOF: 2.37

(c) 3-h Sample:

Site	*Np*	*X*	*y*	*z*	*Atom*	*Occ*	*Beq*
Li1	4	1.00000	0.13709	0.77421	Li	0.8674	1
					Fe	0.1326	1
O3	4	0.77448	0.64890	0.88844	O	2.231	1
Fe1	2	0.00000	0.15870	0.41157	Fe	0.7348	1
					Li	0.2652	1
O1	2	0.00000	0.82258	0.41157	O	1	1
O2	4	0.27807	0.28859	0.76866	O	1	1
Si	2	0.00000	0.84284	0.84102	Si	1	1

Lattice parameters

a (Å)	**6.2754813**
b (Å)	**5.3519562**
c (Å)	**4.9626168**

R_{wp}: 3.81, R_p: 2.90 and GOF: 2.59

(d) 5-h Sample:

Site	*Np*	*X*	*y*	*Z*	*Atom*	*Occ*	*Beq*
Li1	4	0.98778	0.12210	0.80765	Li	0.8953	1
					Fe	0.1047	1
O3	4	0.77511	0.67023	0.89673	O	1	1
Fe1	2	0.00000	0.16656	0.43305	Fe	0.7906	1
					Li	0.2094	1
O1	2	0.00000	0.86883	0.29089	O	1	1
O2	4	0.33543	0.28576	0.80246	O	1	1
Si	2	0.00000	0.80728	0.87672	Si	1	1

Lattice parameters

a (Å)	**6.2829135**
b (Å)	**5.3525385**
c (Å)	**4.9670688**

R_{wp}: 3.73, R_p: 2.73 and GOF: 2.25

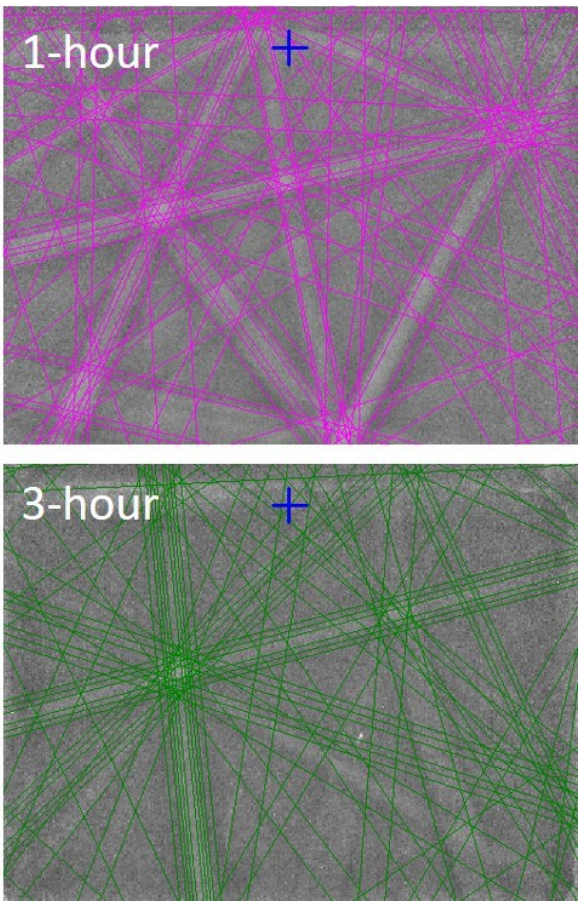

Fig. S10: Electron back scattering (EBSD) images of 1-h milling sample indexed as *Pmn2$_1$* with MAD value of 1.423° and 3-h milling sample indexed as $Pmn2_1$ with MAD value of 1.451°.

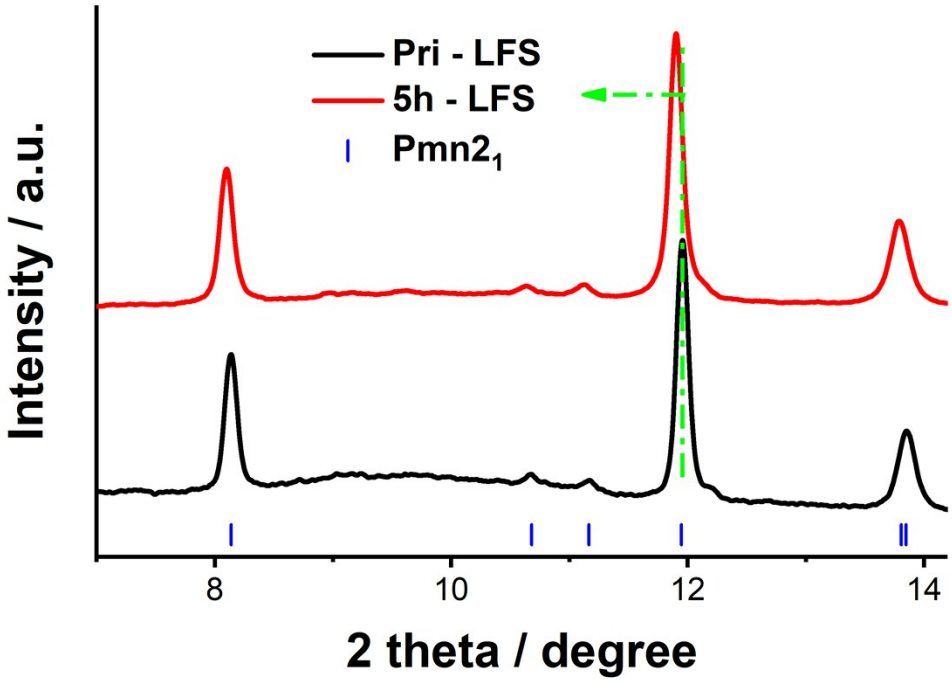

Fig. S11: XRD comparison between pristine ortho-LFS and 5-h milled sample between 8 to 14 degree to determine subtle changes caused by high-energy milling.

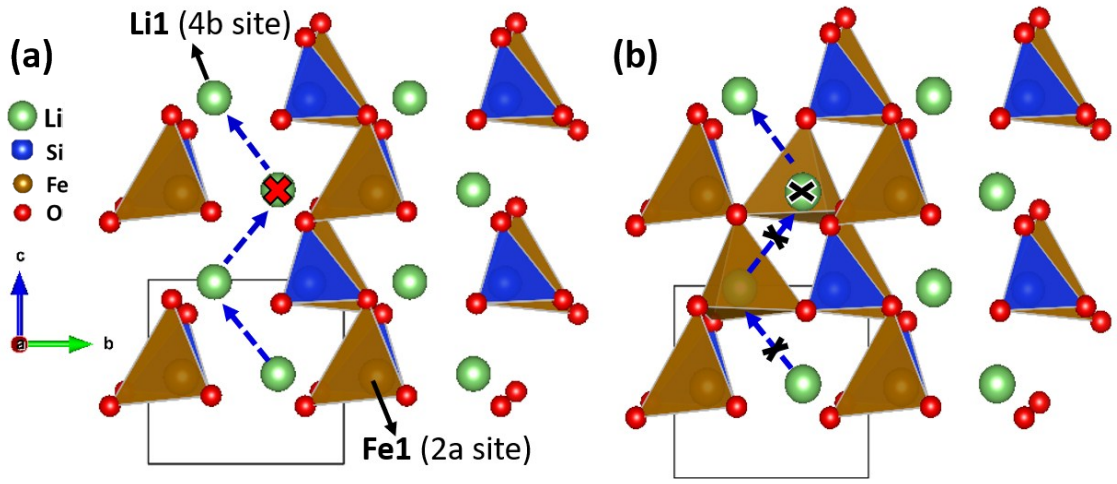

Fig. S12: Illustration of crystal structure of $Pmn2_1$ Li_2FeSiO_4: (a) free of anti-sites and (b) as prepared with Fe_{Li} defects; the lithium pathway (denoted by arrows) is blocked in the latter case. The illustration was created using VESTA software. Li and Fe atoms occupy different crystallographic sites in the ideal *Pmn2₁* structure of Li_2FeSiO_4, denoted as Li1 (4b site) and Fe1 (2a site), respectively [7-8]. During electrochemical lithiation/delithiation, Li migrates in either a-direction (into the paper as denoted by red cross) or a zig-zag c-direction (denoted by blue arrows). When there are significant Fe_{Li} anti-site defects, the lithium diffusion pathway in either a or c direction is blocked as depicted by black cross and arrows.

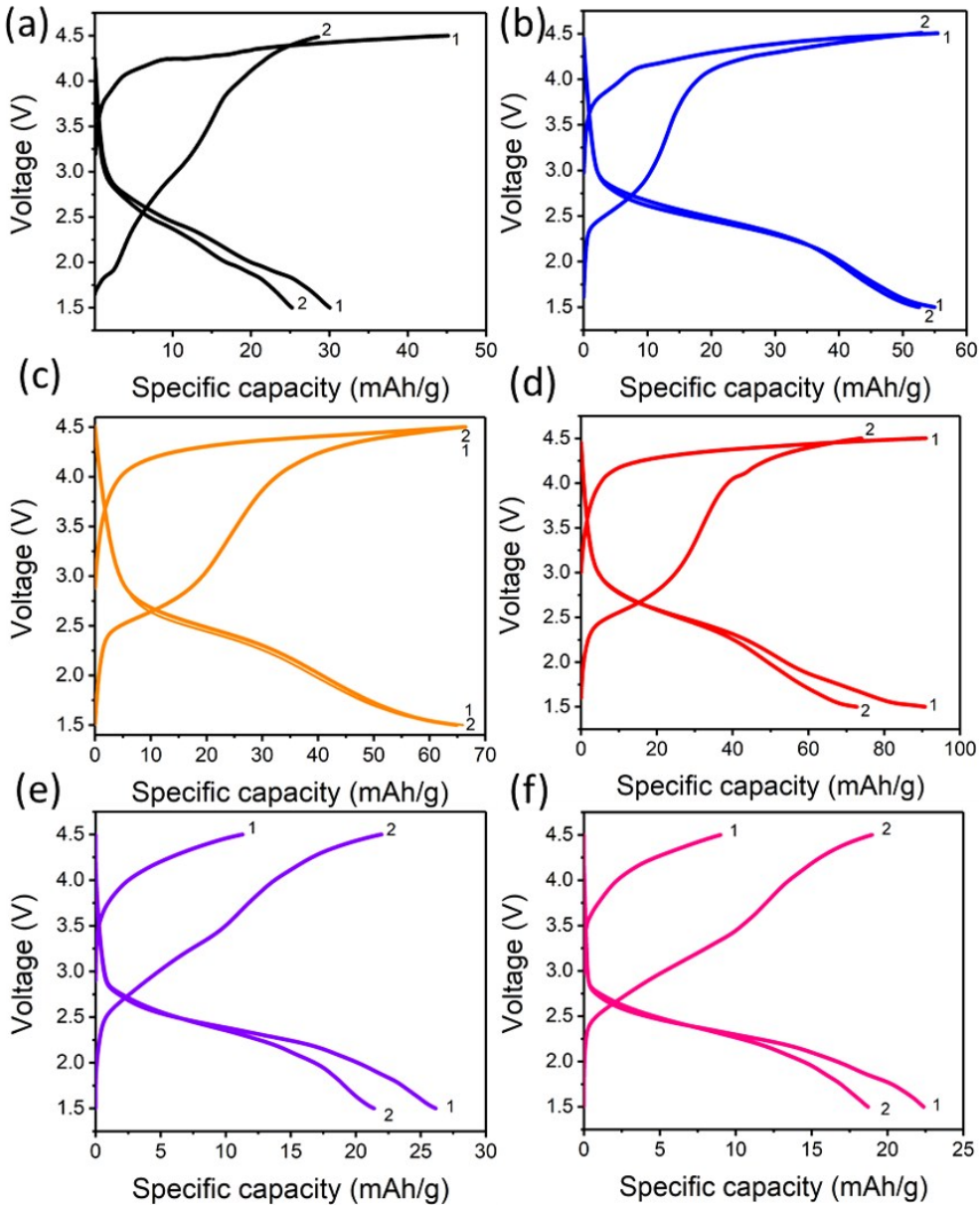

Fig. S13: Galvanostatic charge/discharge of (a) pristine, (b) 1-h, (c) 3-h, (d) 5-h, (e) 8-h and (f) 10-h ortho-LFS samples at C/50 (room temperature) milled materials between 1.5 to 4.5 V vs. Li^+/Li.

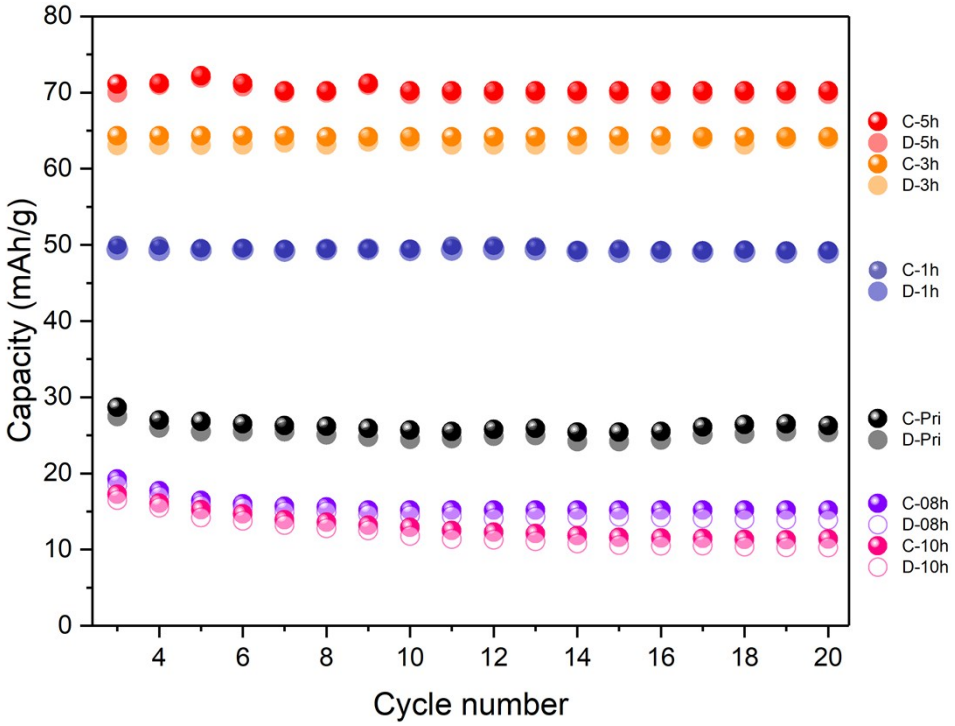

Fig. S14: Specific charge/discharge capacity vs. cycle number of pristine, 1-h, 3-h, 5-h, 8-h and 10-h ortho-LFS samples at C/50 (room temperature) between 1.5 to 4.5V vs. Li^+/Li. For clarity cycle numbers are plotted from 3 cycles onwards as initial cycles (1 and 2) are already plotted in Fig. S13.

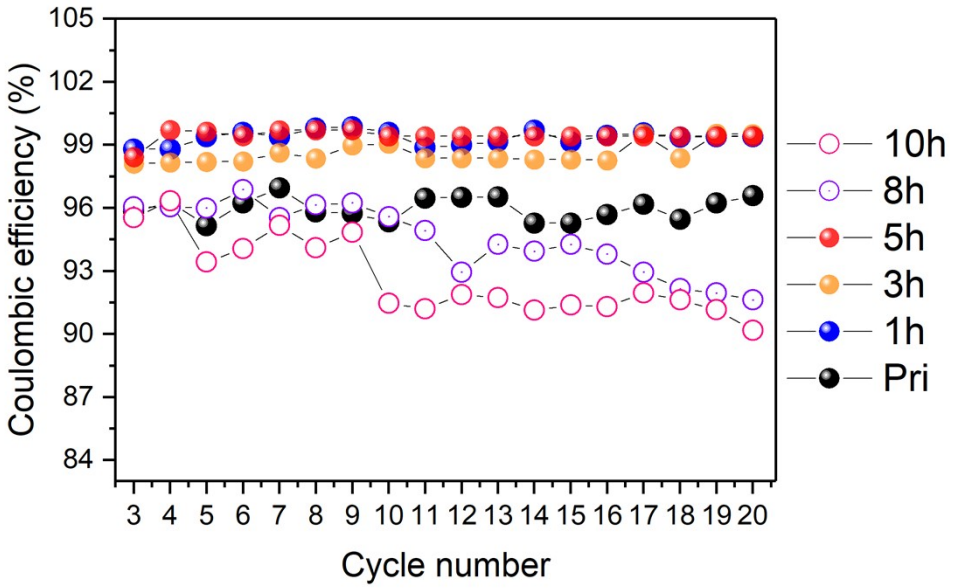

Fig. S15: Coulombic efficiency vs. cycle number of pristine, 1-h, 3-h, 5-h, 8-h and 10-h ortho-LFS samples.

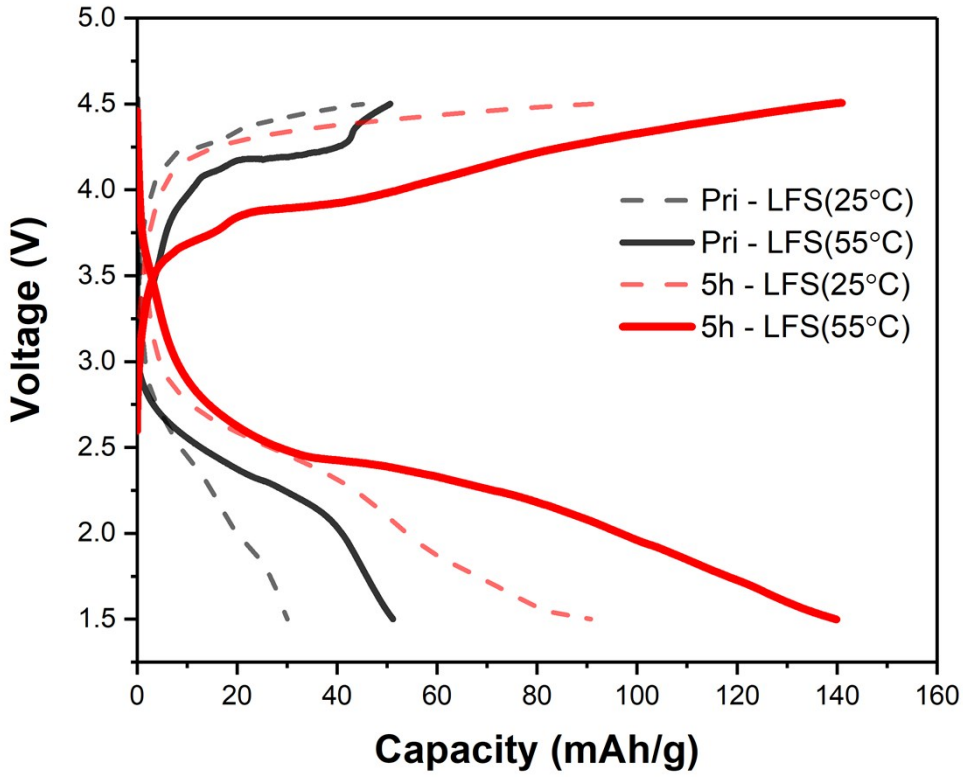

Fig. S16: Comparison of galvanostatic charge/discharge curves of pristine ortho-LFS and 5-h milled samples cycled at C/50 at room temperature and 55 °C from 4.5 to 1.5 V vs. Li^+/Li. Dashed lines are used to denote the samples cycled at RT, while solid lines are used to denote samples cycled at 55 °C, respectively.

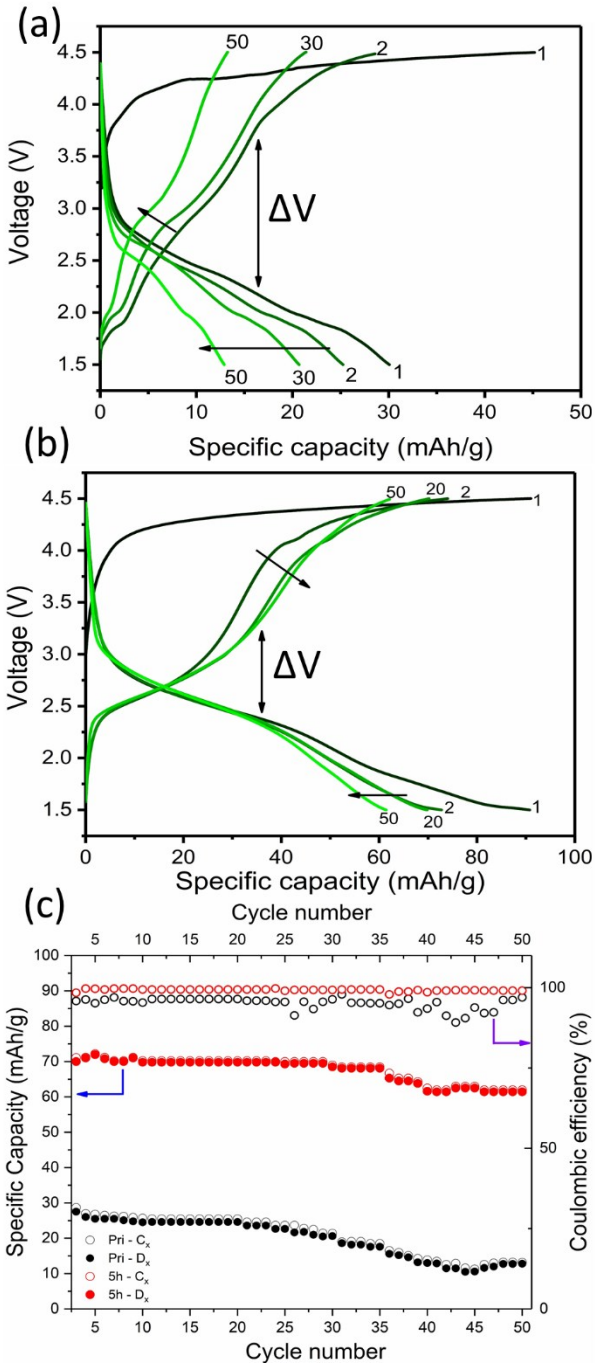

Fig. S17: Galvanostatic charge/discharge curves over 50 cycles (1.5 to 4.5V): Polarization comparison, (a) pristine and (b) 5-h samples. (c) Capacity and Coulombic Efficiency vs. Number of cycles. Cycling at C/50 and RT between 1.5 to 4.5V.

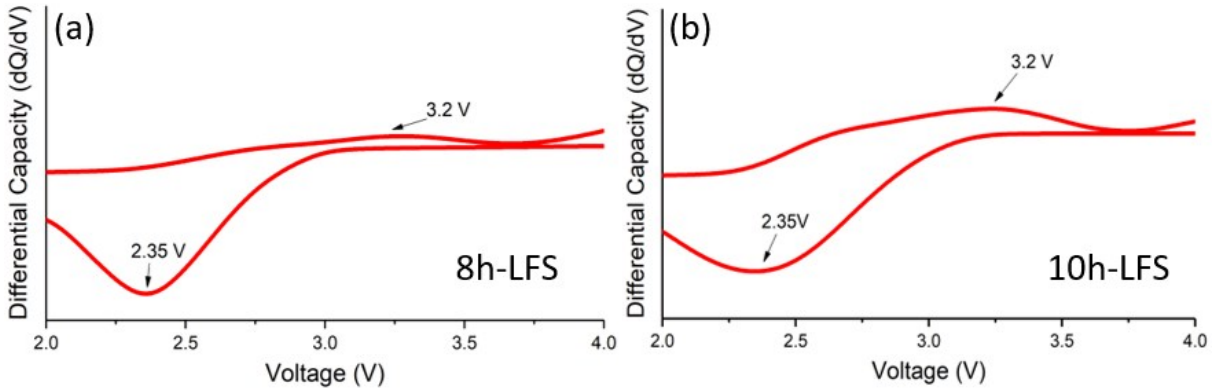

Fig. S18: Differential capacity curves calculated from galvanostatic charge/discharge curves of (a) pristine ortho-LFS and after high-energy milling of (a) 8-h and (b) 10-h.

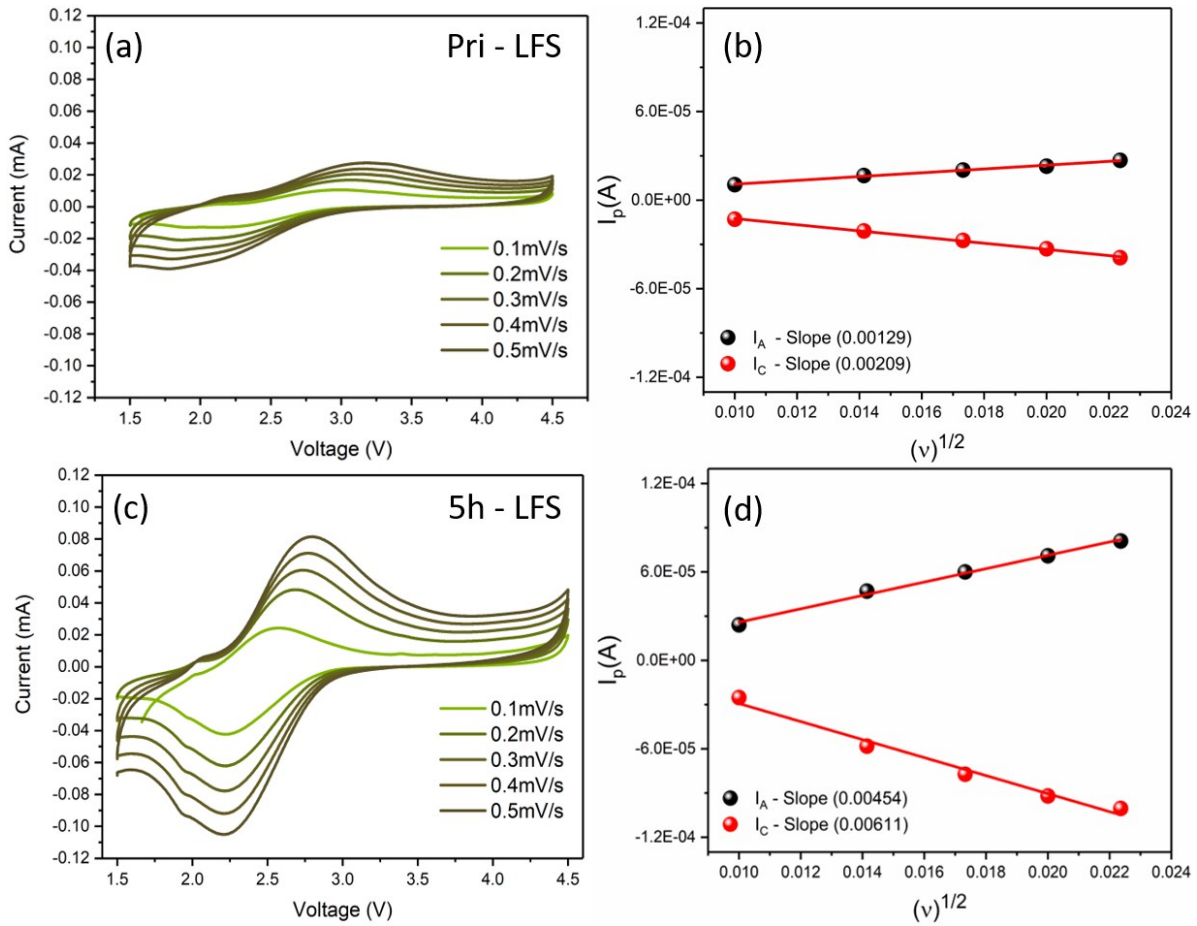

Fig. S19: Cyclic voltammetry scans at different rates for (a) pristine and (c) 5-h samples along corresponding I_p vs. $\nu^{0.5}$ plots in (b) and (d) respectively. The apparent diffusion coefficient (D_{Li}) of lithium ions is estimated from the linear relationship between the peak current (I_p) and the square root of the scan rate ($\nu^{0.5}$) according to the following equations:

$$I_p = 2.69 \times 10^5 \, n^{3/2} \, A \times D^{1/2} \, \nu^{1/2} \, C_{Li}^{\,1/2} \qquad (1)$$

$$D_{Li} = [k / (2.69 \times 10^5 \, n^{3/2} \, A \times C_{Li})]^2 \qquad (2)$$

where I_P (Amps) is the peak current, A (cm^2) is the contact area between electrode and electrolyte, n is the number of electrons involved in redox process, C_{Li}* is the bulk concentration of lithium ions in the electrolyte (0.04 mol cm^{-3} for the Li_2FeSiO_4 cathode), and ν is the scan rate in V/s. Cyclic voltammetry of the pristine and milled samples was performed with scan rates ranging from 0.1 to 0.5 mV/s as shown in Fig. S19a,c. Fig. S19b,d show the peak current has a linear relationship with square root of scan rate, which is a typical behavior for diffusion-controlled processes [9]. The calculated apparent diffusion coefficient is given in Table S3.

Table S3: Calculated apparent diffusion coefficient for pristine and 5-h milled samples obtained by varying the CV scan rates from 0.1 mV/s to 0.5 mV/s.

Sample - D_{Li} (cm^2/s)	Anodic (oxidation)	Cathodic (reduction)
Pri - LFS	2.33×10^{-14}	6.12×10^{-14}
5h - LFS	2.89×10^{-13}	5.23×10^{-13}

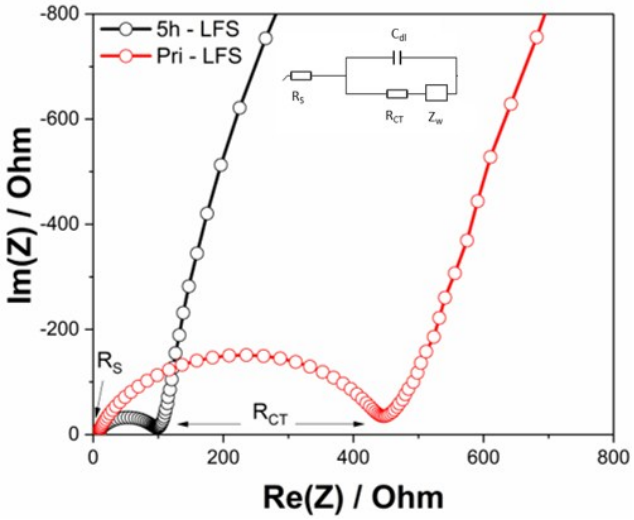

Fig. S20: EIS spectra of pristine and 5-h milled samples. The intercept at the Re(Z) axis represents the ohmic resistance (R_s) of total resistances of electrolyte, separator and electrical contacts. The semicircle relates to the charge transfer resistance (R_{ct}). The inclined line is the Warburg impedance (Z_W), which is associated with Li^+ ion diffusion in the cathode active particles [10]. The EIS curves were fitted by an equivalent circuit with the aid of EC-Lab software (see inset of Fig. S20). The fitting results are presented in Table S4 below. R_{CT} is significantly less for the 5-h sample than the corresponding one for pristine sample exemplifying the enhanced intercalation kinetics induced as result of the mechanochemical annealing effect confirming our CV results reported in Fig. S19.

Table S4: EIS fitting results for pristine and 5-h milled samples.

Sample	R_S (Ω)	R_{CT} (Ω)
Pri - LFS	10.2	412.5
5h - LFS	8.3	78.6

References:

1. Brame, J.; Griggs, C. *Surface Area Analysis Using the Brunauer-Emmett-Teller (BET) Method: Standard Operating Procedure Series: SOP-C*; US Army Engineer Research and Development Center-Environmental Laboratory …: 2016.

2. Zhou, M.; Wei, Z.; Qiao, H.; Zhu, L.; Yang, H.; Xia, T., Particle size and pore structure characterization of silver nanoparticles prepared by confined arc plasma. *J. Nanomater.* **2009,** *2009*, 3.

3. Brodusch, N.; Demers, H.; Gauvin, R., The f-Ratio Method for X-Ray Microanalysis in the SEM. In *Field Emission Scanning Electron Microscopy*, Springer: 2018; pp 55-65.

4. Da Silva, K. L.; Menzel, D.; Feldhoff, A.; Kübel, C.; Bruns, M.; Paesano Jr, A.; Düvel, A.; Wilkening, M.; Ghafari, M.; Hahn, H., Mechanosynthesized $BiFeO_3$ nanoparticles with highly reactive surface and enhanced magnetization. *J. Phys. Chem. C* **2011,** *115* (15), 7209-7217.

5. Zhang, Q.; Liu, S.-J.; Yu, S.-H., Recent advances in oriented attachment growth and synthesis of functional materials: concept, evidence, mechanism, and future. *J. Mater. Chem.* **2009,** *19* (2), 191-207.

6. Li, M.; Schnablegger, H.; Mann, S., Coupled synthesis and self-assembly of nanoparticles to give structures with controlled organization. *Nature* **1999,** *402* (6760), 393.

7. Liivat, A.; Thomas, J. O., Li-ion migration in Li_2FeSiO_4-related cathode materials: A DFT study. *Solid State Ionics* **2011,** *192* (1), 58-64.

8. Armstrong, A. R.; Kuganathan, N.; Islam, M. S.; Bruce, P. G., Structure and Lithium Transport Pathways in Li_2FeSiO_4 Cathodes for Lithium Batteries. *J. Am. Chem. Soc.* **2011,** *133* (33), 13031-13035.

9. Denis, Y.; Fietzek, C.; Weydanz, W.; Donoue, K.; Inoue, T.; Kurokawa, H.; Fujitani, S., Study of $LiFePO_4$ by cyclic voltammetry. *J. Electrochem. Soc.* **2007,** *154* (4), A253-A257.

10. Levi, M.; Salitra, G.; Markovsky, B.; Teller, H.; Aurbach, D.; Heider, U.; Heider, L., Solid-State Electrochemical Kinetics of Li-Ion Intercalation into $Li_{1-x}CoO_2$: Simultaneous Application of Electroanalytical Techniques SSCV, PITT, and EIS. *J. Electrochem. Soc.* **1999,** *146* (4), 1279-1289.